

# **Application of a microstructural characterization uncertainty quantification framework to Widmanstätten $\alpha$ -laths in additive manufactured Ti-6Al-4V**

Gregory T. Loughnane<sup>1</sup>, Sarah L. Kuntz<sup>1</sup>, Nathan Klingbeil<sup>1</sup>, John M. Sosa<sup>2</sup>, Jeff Irwin<sup>3</sup>, Abdalla R. Nassar<sup>4</sup>, Edward W. Reutzel<sup>4</sup>

<sup>1</sup> Dept. of Mechanical and Materials Engineering, Wright State Univ., Dayton, OH 45435

<sup>2</sup> Center for Electron Microscopy and Analysis, The Ohio State Univ., Columbus, OH 43212

<sup>3</sup> Dept. of Mech. and Nuclear Engineering, The Pennsylvania State Univ., Univ. Park, PA 16802

<sup>4</sup> Applied Research Laboratory, The Pennsylvania State Univ., Univ. Park, PA 16802

REVIEWED

## **1 Abstract**

This work applies statistical analysis and uncertainty quantification tools developed for characterizing virtual microstructures in three dimensions to a two-dimensional experimental investigation of Ti-6Al-4V Widmanstätten  $\alpha$ -lath thicknesses obtained from back-scattered electron (BSE) or electron back-scatter diffraction (EBSD) images on two thin-walled samples manufactured via the LENS® process. The Materials Image Processing and Automated Reconstruction (MIPAR™) software optimizes unique recipes for conversion of the BSE or EBSD images to binary data, and subsequently computes the inverse of the linear intercept for each  $\alpha$ -lath. Mean  $\alpha$ -lath thicknesses and discrete probability density functions (PDFs) of inverse intercepts are used to make quantitative comparisons of  $\alpha$ -lath structures at different heights throughout the thin walls. Real-time thermal data collected during the LENS® experiment is then compared to quantitative microstructural results in order to determine trends between  $\alpha$ -lath structures, thermal gradients, and melt pool areas across experimental process parameters.

## **2 Introduction**

Direct metal additive manufacturing (AM) refers to any process that manufactures near-net shape components via direct deposition of metallic material into a pool of molten metal. These processes differ primarily in the power source (laser- or electron-beam) and feedstock delivery system (powder stream, wire feed, powder bed). For each type of process, microstructural characterization techniques are used to assess and qualify the strength, reliability, and overall quality of metallic components. Further, while AM has advantages over traditional machining processes, such as lead time improvements and lower per-unit costs for relatively small batches, the inherent temperature variability in all cyclic direct metal AM processes often results in inconsistent and undesirable solidification microstructures.

One approach for understanding temperature- and solidification microstructure-variability in direct metal AM is a method termed “process mapping” developed by Beuth et al. [1]. This

methodology maps process outcomes in terms of process variables, where variables represent experimentally-controlled factors such as beam power and velocity and outcomes refer to experimental results such as stress or microstructural characteristics. The idea behind the process mapping approach is to allow all direct metal AM processes, which act in different regions of processing space, to be characterized and analyzed in a cohesive way. Early work focused on residual stress in metal and polymer AM processes [2-6]. Subsequent work investigated control of melt pool dimensions under steady state conditions for the full range of the Laser Engineering Net Shaping (LENS®) process through investigation of nondimensional thermal metrics [7-9]. This work was extended to provide direct predictions of solidification microstructure [10,11]. Additionally, many process mapping approaches have leveraged analytical and thermal finite element models to predict cooling rates and thermal gradients, parameters that are used to predict trends in solidification microstructures [12-16]. Further, within recent years, detailed microstructural observations have shown correspondence to theoretically calculated melt pool geometries for given sets of process variables [17-18].

Real-time sensing and adaptive control utilizes process mapping techniques by monitoring deposition and altering process variables in order to maintain constant melt-pool geometry or alternatively to control component build parameters. Over the years, significant research regarding adaptive control of laser processes has been conducted in which monitoring methods are based on the physical phenomena that occur due to laser-materials interaction (see Ref. [19] for a recent thorough review). Many of the techniques and sensors used for investigation of AM processes have historically been used for laser cladding and welding processes (i.e. optical and acoustic techniques). For laser AM processes, researchers have leveraged optical imaging techniques to monitor temperature during laser-based manufacturing of various materials [20]. Griffith et al. studied melt-pool temperatures and gradients collected during deposition of H13 tool steel [21], and Hofmeister et al. achieved significant stabilization of melt-pool size via control of laser power in 316 stainless steel through use of an optical thermal imaging system [22]. Correlation of thermal data to solidification microstructure has also been a topic of interest for various materials, including 316 stainless steel [23] and Ti-6Al-4V [24-26, 27-28]. However, most microscale observation of AM components is qualitative in nature and does not lend itself to the process mapping approach.

In contrast, this work seeks to provide a methodology for the quantitative analysis of AM Ti-6Al-4V sub-grain level microstructures, using two thin-walled L-shaped components built via the LENS® process, and leveraging techniques similar to those utilized for quantifying the average size of Widmanstätten  $\alpha$ -laths in forged billets of Ti-6Al-4V [29]. The Materials Image Processing and Automated Reconstruction (MIPAR™) [30] software was used to optimize recipes for conversion of back-scattered electron (BSE) and electron back-scatter diffraction (EBSD) images into binary data suitable for mean linear intercept (MLI) [31] analysis and thus  $\alpha$ -lath thickness calculations. In addition, a quantitative comparison technique for  $\alpha$ -laths observed in different regions of the two components is presented, where discrete PDFs of MLIs are compared for geometric similarity via a Modified version of the Bhattacharyya Coefficient

(MBC) [32]. Lastly, quantitative  $\alpha$ -lath data is analyzed for trends relative to the real-time thermal data collected during the 3D directed energy deposition experiment used to create the two thin walls. Kriczky et al. published an overview of the experiment [33] and this work compares thermal gradients and melt-pool areas to  $\alpha$ -lath thicknesses in the resulting solidification microstructure for both thin-walled L-shaped components.

### 3 Additive Manufacturing and Thermal Imaging of Ti-6Al-4V Components

The LENS<sup>TM</sup> system used to build components investigated in this work represents a collaborative effort between Penn State University's Center for Innovative Metal Processing through Direct Digital Deposition (CIMP-3D), Stratonics, and Optomec. The integrated multi-sensor/process model-based control system leverages an Optomec MR-7 LENS<sup>TM</sup> system, outfitted with a Stratonics ThermaViz<sup>®</sup> thermal imaging camera. Using the integrated system, CIMP-3D manufactured the two relatively-large (~50 mm tall), L-shaped, thin-wall samples of AM Ti-6Al-4V, shown in Figure 1. Each sample is composed of two legs; the first leg is constructed from a single bead, while the second has three beads per layer. The key difference between these samples is the dwell time used between added material layers. One sample was built with zero dwell time between layers, while the other sample had a dwell time of four seconds. These two samples are shown in Figure 1A and Figure 1B, respectively.

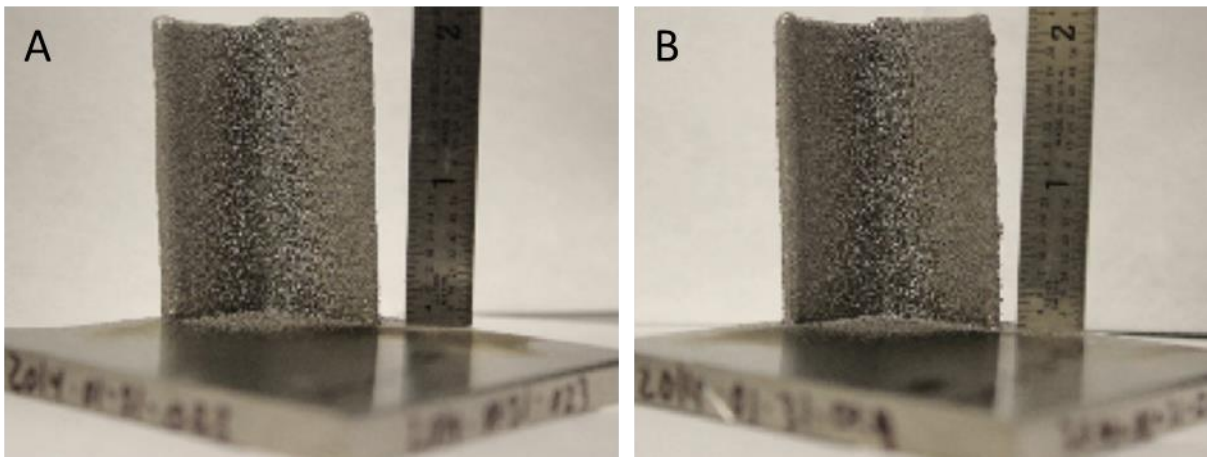


**Figure 1: AM Ti6Al-4V components constructed using the LENS<sup>TM</sup> process: L-shaped thin-walled samples under investigation; 0 s dwell (A), and 4 s dwell (B) [33].**

The complete thermal history of each component was captured in real time during the experiment. Detailed information regarding the step-by-step procedures to transform point-by-point thermal data into thermal gradients, melt pool areas and the like is available in [33] for the interested reader. Here, only the authors' designations for the lower 10%, upper 90%, and center 33% are of interest for both the 1- and 3-bead legs of each sample; these designations are illustrated using the zero second dwell specimen shown in Figure 2. For this work,  $\alpha$ -lath data

was collected for both legs of each sample (0s dwell, 4s dwell) within the center 33% region and along the entire height of the thin walls (z-direction as pictured below).

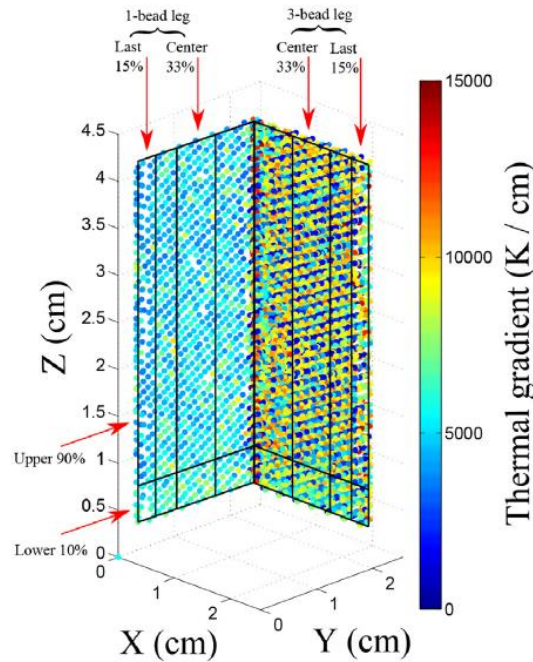


**Figure 2: Thermal gradient reconstruction showing spatial designations for AM Ti-6Al-4V components:** Isometric 3D reconstruction of calculated thermal gradients for the zero second dwell sample [33].

#### 4 Microstructural Characterization of Ti-6Al-4V $\alpha$ -laths

In alpha-beta titanium alloys such as Ti-6Al-4V, the body-centered cubic (BCC)  $\beta$  (beta) phase transforms to a hexagonally close packed (HCP)  $\alpha$  (alpha) phase upon cooling through the  $\beta$  transus, which occurs at approximately 1270° K [35]. The smaller  $\alpha$  features of Ti-6Al-4V begin growing within the metastable  $\beta$  phase from grain boundaries to produce  $\alpha$  lamellae/laths within a  $\beta$  matrix. The overall  $\alpha$ + $\beta$  morphology that results is called the Widmanstätten morphology, which can take two forms: colony or basketweave  $\alpha$ . In AM processes, depending on part geometry and AM process parameters, cooling rates can vary significantly across a single part, especially in between added layers and on the edges of parts. As a result, multiple  $\alpha$  structures are often observed in single  $\beta$  grains, as exemplified in Figure 3 which shows two BSE images depicting colony- and basketweave- $\alpha$  in the same field of view. While microstructural variation is characteristic of the LENS<sup>TM</sup> samples under investigation, such inconsistent microstructure does not lend itself to rapid qualification methods for AM nor does it make quantifying microstructural features using existing toolsets a straightforward task.

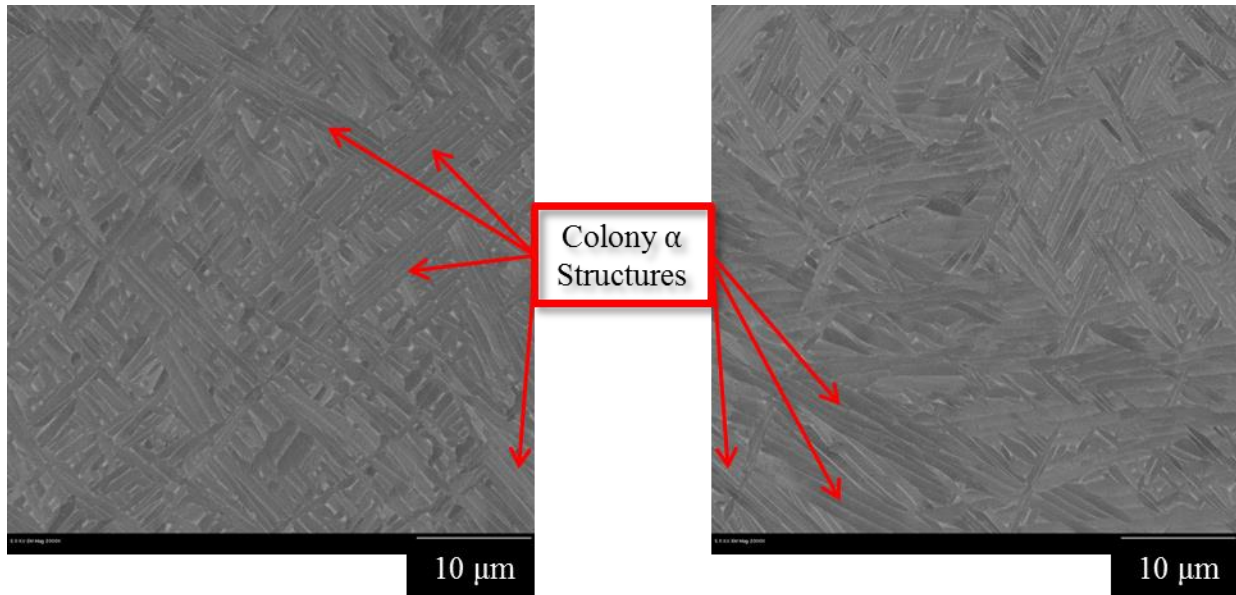


**Figure 3: Colony and basketweave  $\alpha$  microstructures observed in LENS<sup>TM</sup> Ti-6Al-4V:** BSE image showing colony  $\alpha$  microstructures present amidst a majority of basketweave  $\alpha$ ; observed in the 1-bead leg of the sample with zero dwell time between layers.

Inspection of both samples and their solidification microstructures resulted in a designation of five zones along the height of each sample, as pictured in Figure 4 below. Additionally, this inspection yielded the best way to image  $\alpha$ -laths of various sizes. For all sizes, very fine polishing and thorough cleaning was required, however the mode of data collection changed for different lath sizes. For thicker laths like those pictured in Figure 3, back-scattered electron (BSE) imaging at a magnification of 2000x (working distance 5 mm, accelerating voltage 20 kV) proved to be a repeatable methodology. However, smaller laths required crystallographic analysis via electron back-scatter diffraction (EBSD) (step size 0.1  $\mu\text{m}$ ) to be distinguishable.

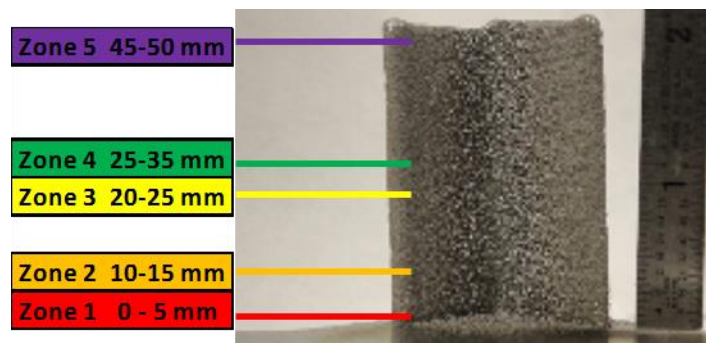


**Figure 4: Zones 1-5 used for  $\alpha$ -lath width analysis:** Spatial locations along the sample height for zone designations used in  $\alpha$ -lath width analysis.

Zones 2, 3, and 4, those not located at the extreme ends of the sample (top, bottom), appeared to have steady state microstructures. More specifically, the central zones along the

height of the thin walls appeared to have qualitatively similar lath sizes, which can be seen in Figure 5. However, zones 1 and 5 were very difficult to image using BSE techniques, and produced BSE images unsuitable for image processing. As a result EBSD data was required, as shown in Figure 6. The laths requiring EBSD appear smaller based on the more acicular nature of the observed  $\alpha$ -microstructure.

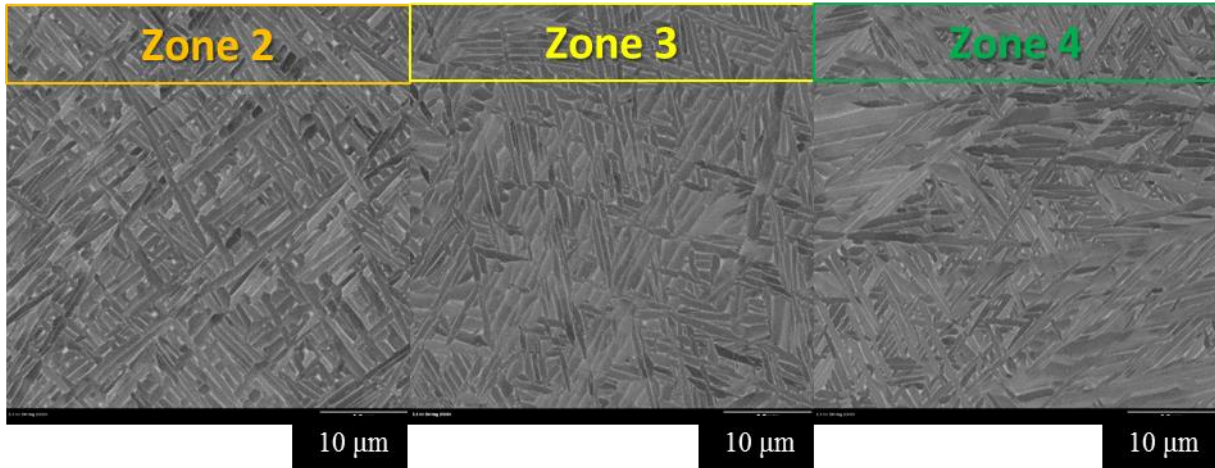


**Figure 5: Steady state zones of AM Ti-6Al-4V components:** BSE images of zones 2, 3, and 4 showing easily quantifiable basketweave  $\alpha$  structures; taken from the 1-bead leg of the sample with zero dwell time between layers.

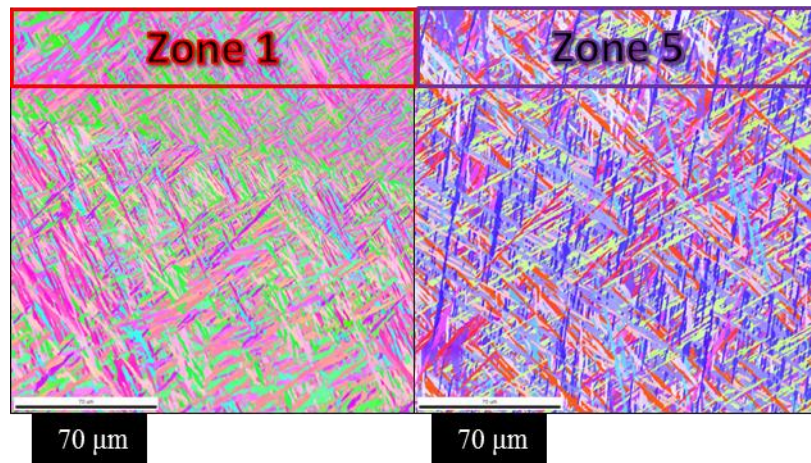


**Figure 6: Top and Bottom Zones of AM Ti-6Al-4V components, EBSD Imaging:** EBSD images of zones 1 and 5 showing more acicular microstructures than those in other zones; taken from the 1-bead leg of the sample with zero dwell time between layers.

## 5 Image Processing via MIPAR™

Lath thicknesses and distributions are determined using the image analysis software MIPAR™ (Materials Image Processing and Automated Reconstruction) [30], developed by Sosa, et al. at The Ohio State University. For each imaging technique, a series of image

processing steps was completed within MIPAR™ to convert the data into binary images for quantification.

For BSE imaging in steady state zones, a 6-step series of image filtering techniques was implemented to convert grayscale images to binary, as shown in Figure 7. In particular the following series of filters was used to segment features: Wiener filter, Fast Fourier Transform filter, adaptive threshold, dilation, erosion, and feature rejection. Although filter choices were based on experience and trial-and-error, the optimum parameters for each filter were objectively determined based on segmentation-to-image mutual information for each image-processing algorithm used in the sequence (see Ref [30] for details).

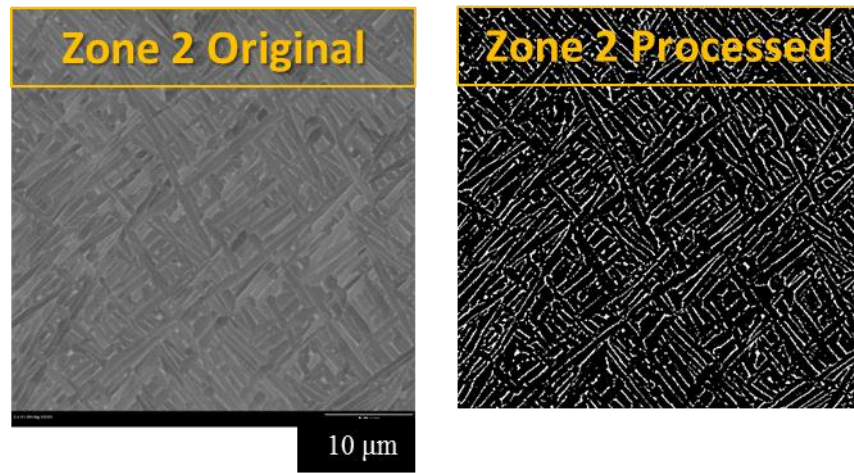


**Figure 7: BSE image filtering for steady state zones:** Example of a BSE image converted to binary for  $\alpha$ -lath width analysis using MIPAR™.

Colored EBSD images were converted to grayscale from their default RGB format by adding (R+G+B) content for each pixel. Similarly to the images in the steady state zones, a unique multi-step image-processing sequence was developed. Specifically, a median filter and edge find sequence was applied for three rounds, followed by a final erosion and feature rejection, producing binary data as shown in Figure 8. Optimum filter parameters were again determined based on segmentation-to-image mutual information.

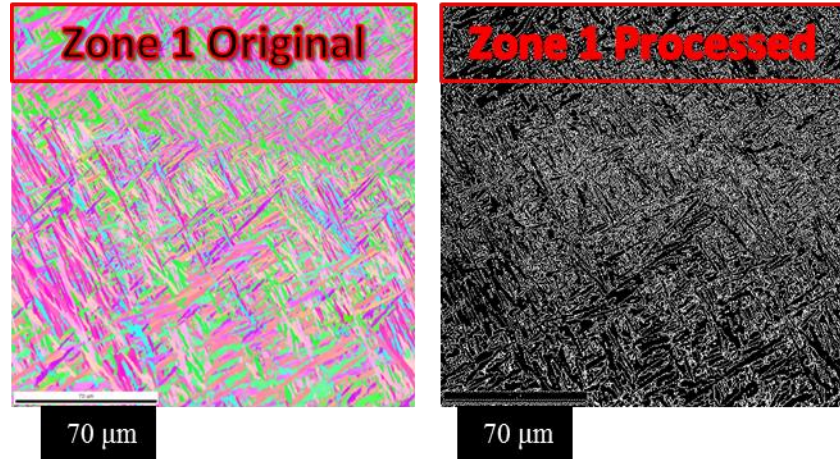


**Figure 8: EBSD image filtering for top and bottom zones:** Example of an EBSD image converted to binary for  $\alpha$ -lath width analysis using MIPAR™.

## **6 Determining $\alpha$ -lath Thicknesses and Quantifying Uncertainty in Microstructure**

Having obtained binary images from the microstructural data, Widmanstätten  $\alpha$ -lath thicknesses were calculated via the mean inverse of the linear intercept [31], a procedure also performed within MIPAR™. This method superimposes a grid of parallel lines on the image, subsequently rotates the grid by  $10^\circ$  increments to collect measurements in multiple directions, and records linear intercepts ( $\lambda$ ) and inverse intercepts ( $1/\lambda$ ) computed for each lath (see [29,31]) so that the true 3D thickness of  $\alpha$ -laths can be estimated via Eq. (1).

$$thickness = \frac{1}{1.5(1/\lambda)_{mean}} \quad (1)$$

The application of this method approximates laths as layered structures and estimates the true thickness of a series of “infinite” plates of finite thicknesses (i.e. finite only in 1 dimension). Further, it works best for more randomly oriented (i.e. 100% basketweave) structures; thus the  $\alpha$  colonies visible in Figure 3 provide an additional source of uncertainty in these measurements.

Average lath thicknesses, computed for each image and averaged based on the number of images taken for each section are shown in Table 1 below. The confidence intervals were computed using Student’s t-distribution on (n-1) degrees of freedom as a benchmark with a significance level of 0.05 to produce two-sided 95% confidence bounds. In all cases, the calculated  $\alpha$ -lath thicknesses are larger in the steady state region than in the top and bottom regions; further, the bottom regions produce a smaller average thickness than the top regions.

**Table 1: Average  $\alpha$ -lath thickness comparison:** Comparison of average  $\alpha$ -lath thicknesses for all zones across each leg of both samples, along with 95% confidence intervals based on the number of images collected.

	Zone	$\alpha$ -Lath Width (microns)	95% Confidence Interval	# Images
<b>0s Dwell 1-Bead Leg</b>	1	0.55	n/a	1
	2	0.58	0.14	5
	3	0.69	0.03	5
	4	0.67	0.26	2
	5	0.59	n/a	1
<b>0s Dwell 3-Bead Leg</b>	1	0.54	n/a	1
	2	0.94	0.10	5
	3	0.92	0.06	5
	4	1.00	0.14	5
	5	0.58	n/a	1
<b>4s Dwell 1-Bead Leg</b>	1	0.32	n/a	1
	2	0.35	0.07	4
	3	0.41	0.06	5
	4	0.30	0.02	5
	5	0.53	n/a	1
<b>4s Dwell 3-Bead Leg</b>	1	0.50	n/a	1
	2	0.68	0.12	5
	3	0.66	0.16	5
	4	0.77	0.13	5
	5	0.58	n/a	1

In addition to quantifying mean  $\alpha$ -lath thickness, consideration is given to the variability between entire distributions of inverse intercept length, which are taken to represent the lath microstructure observed in each binary image. Inverse intercept distributions are constructed using all inverse intercepts calculated for the set of images collected in each zone (see Table 1 above for the number of images collected in each set). Discrete distributions are binned using a 30-bin scheme between 0 and 5 that was based on the observed data, which typically ranged between 0 and 5. The larger-valued outliers (corresponding to extremely small alpha lath widths) inherently result from this analysis due to complicated three-dimensional basketweave microstructure being observed in only two dimensions, although imperfect binary representations likely play a role as well. Once constructed, the distributions within the zones of each sample leg are compared for geometric similarity via a Modified version of the Bhattacharyya Coefficient (MBC) [32], which is applied to discrete PDFs via Eq. (2).

$$MBC = \sqrt{1 - \sum_{i=1}^n \sqrt{R_i S_i}} \quad (2)$$

In Eq. (2)  $R_i$  and  $S_i$  correspond to the fraction of inverse intercept data contained in bin  $i$  for the discrete probability distributions (i.e., histograms)  $R$  and  $S$ , and correspond to the two distributions being compared. For this work, distributions are compared within sample-leg steady state zones (i.e. zone 2 to 3, zone 2 to 4, and zone 3 to 4) as well as between sample-leg top and bottom zones (i.e. zone 1 to 5). Comparing BSE and EBSD results separately ensure that no aliasing effects occur based solely on variations in data collection procedures and image processing techniques.

Although other methods of discrete distribution comparisons exist, the MBC was selected for its relatively high sensitivity to subtle variations in the PDFs. Additionally the MBC statistic ranges between 0 and 1, where a value of 0 implies that two models are identically distributed, and higher values imply greater variance between distributions. For reference, previous work by this author has shown that an  $MBC \leq 0.13$  produces qualitatively well-matched distributions [34].

For each leg, MBC calculations between zones are shown in Table 2. MBC values above the threshold of 0.13 are highlighted in red, and in each of these cases a clear qualitative difference in microstructure can be observed in BSE or EBSD images. The highest MBC in Table 2, corresponding to a comparison of zone 1 vs. 5 in the 1-bead leg of the 4s dwell sample, was determined to be attributable to poor data collection quality of the EBSD scan used for analysis of zone 1.

**Table 2: MBC comparisons of inverse intercept distributions:** MBC calculations for each sample leg, comparing top and bottom regions as well as steady state zones.

	1-Bead Leg, 0s Dwell	1-Bead Leg, 4s Dwell	3-Bead Leg, 0s Dwell	3-Bead Leg, 4s Dwell
<b>Zone 1 - Zone 5</b>	0.045	<b>0.328</b>	0.097	0.092
<b>Zone 2 - Zone 3</b>	<b>0.195</b>	0.072	0.045	0.041
<b>Zone 2 - Zone 4</b>	<b>0.189</b>	0.092	0.043	0.074
<b>Zone 3 - Zone 4</b>	0.029	<b>0.152</b>	0.075	0.103

Distributions of inverse intercept length can also be analyzed graphically for each leg. For brevity, only the 1-bead leg zero second dwell case is shown in Figs. 9-10. Zones 3 and 4, as well as zones 1 and 5 appear to have significant similarities, respectively. These conclusions are supported by the data in Table 2 above, where the comparison of zones 3 and 4 produces an  $MBC = 0.029$  and zone 1 to zone 5 produces and  $MBC = 0.045$ , both providing values well below the threshold of  $MBC \leq 0.13$ . Notably, these zones had extremely similar lath thicknesses, 0.69 vs. 0.67  $\mu\text{m}$  for zone 3 vs. 4 and 0.55 vs. 0.59  $\mu\text{m}$  for zone 1 vs. 5. Further parallels can be

drawn with the lath thickness data in Table 1. In particular, the distributions with higher fractions at smaller inverse intercepts are those with larger lath thicknesses.

Interestingly, the inverse intercept lengths observed in particular bins of zones 1 and 5 for each leg produced distributions that were not smooth in certain ranges (see Figure 10). This occurred for all zone 1 and 5 data, and is perhaps due to the image processing routines used for analysis; however this is a bias left for investigation in future work.

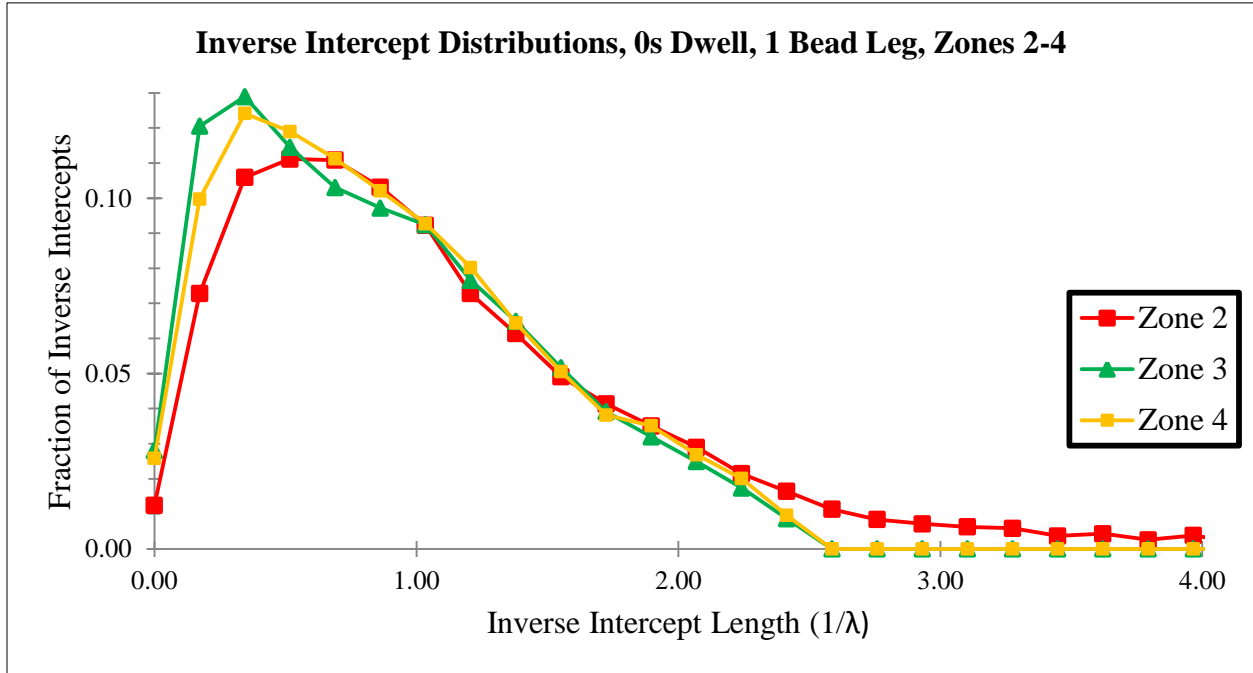


**Figure 9: Inverse intercept distributions, zones 2-4, 0s dwell, 1-bead leg:  $1/\lambda$  distributions plotted between 0 and 4.**

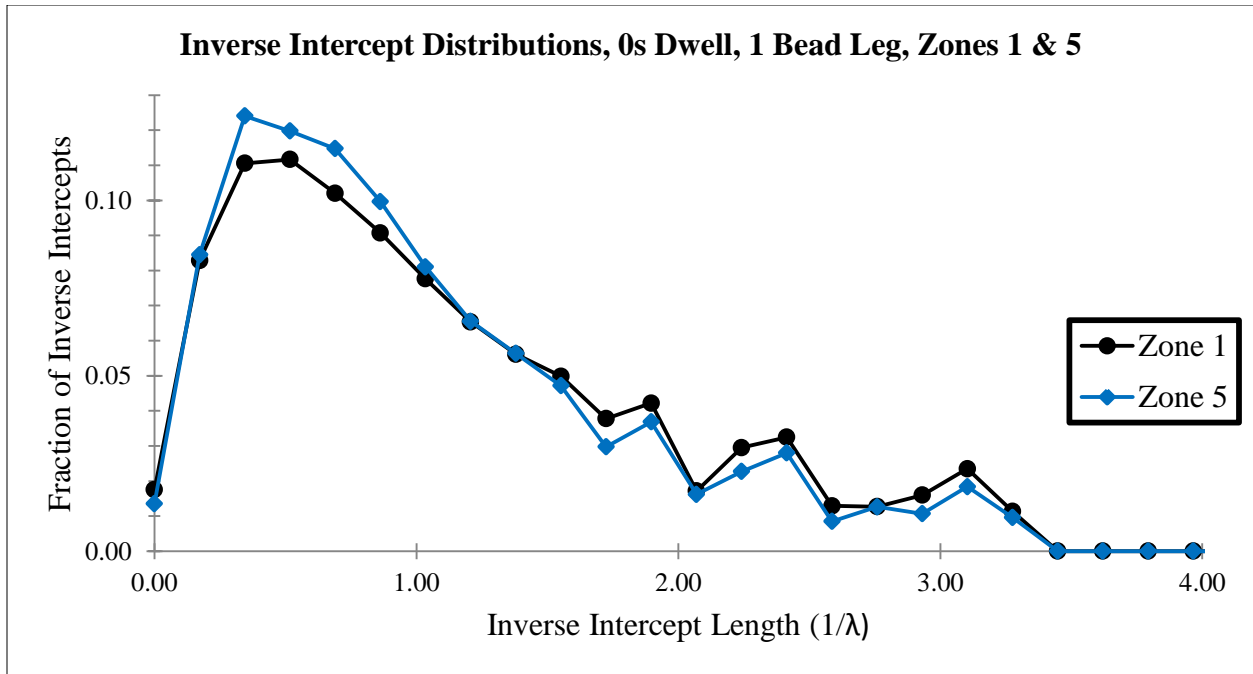


**Figure 10: Inverse intercept distributions, zone 1 vs. 5, 0s dwell, 1-bead leg:**  $1/\lambda$  distributions plotted between 0 and 4.

### **7 Comparison of Widmanstätten $\alpha$ -lath Widths to Thermal Imaging Data**

Lastly, a comparison of the quantitative  $\alpha$ -lath thicknesses to the thermal imaging data provided in Ref [33] is in order. For these comparisons, zones 2-5 are grouped to correspond to the upper 90% region of the thermal imaging data, leaving zone 1 to represent the lower 10%. All microstructural analysis was completed within in the center 33% of each leg of the samples (see Figure 2 for reference), so Region 1 is designated as the lower 10% and center 33% area of the samples (i.e. zone 1) while Region 2 is the upper 90% and center 33% of the samples (i.e. zones 2-5).

Table 3 shows a comparison across build regions, including averages for thermal gradients, melt pool areas and  $\alpha$ -lath thicknesses, Table 4 shows a comparison between dwell times, and Table 5 compares each of these metrics using the number of beads per layer.

**Table 3: Comparison of thermal gradient, melt pool area, and  $\alpha$ -lath thickness across build regions:** This table compares the lath thicknesses in zone 1 to the lower 10% thermal data and the average of lath thicknesses observed in zones 2-5 to the upper 90% thermal data.

			Region 1	Region 2	Comparison
0 sec	Thermal Gradient [K/cm]	1 Bead	6047	5112	Higher for Region 1
		3 Bead	6177	6469	Higher for Region 2
	Melt Pool Area [mm <sup>2</sup> ]	1 Bead	2.53	2.71	Larger for Region 2
		3 Bead	1.27	1.59	Larger for Region 2
	$\alpha$ -lath Width [ $\mu$ m]	1 Bead	0.56	0.64	Thicker for Region 2
		3 Bead	0.54	0.86	Thicker for Region 2
4 sec	Thermal Gradient [K/cm]	1 Bead	7061	6630	Higher for Region 1
		3 Bead	6925	6893	Higher for Region 1
	Melt Pool Area [mm <sup>2</sup> ]	1 Bead	2.53	2.76	Larger for Region 2
		3 Bead	1.10	1.23	Larger for Region 2
	$\alpha$ -lath Width [ $\mu$ m]	1 Bead	0.33	0.41	Thicker for Region 2
		3 Bead	0.41	0.67	Thicker for Region 2

**Table 4: Comparison of thermal gradient, melt pool area, and  $\alpha$ -lath thickness across dwell times:** This table compares the averages of lath thicknesses observed in zones 1-5 for both 1- and 3-bead legs to average thermal data for each dwell time used in the samples.

	0 sec	4 sec	Comparison
Thermal Gradient [K/cm]	5823	6795	Thermal gradient increases with pause length
Melt Pool Area [mm <sup>2</sup> ]	2.39	2.19	Melt pool area decreases with pause length
$\alpha$ -lath Width [ $\mu$ m]	0.71	0.51	$\alpha$ -lath thickness decreases with pause length

**Table 5: Comparison of thermal gradient, melt pool area, and lath thickness across number of beads:** This table compares the averages of lath thicknesses observed in zones 1-5 for both 0s and 4s dwell times to average thermal data for 1- and 3-bead legs of the samples.

	1 Bead	3 Bead	Comparison
Thermal Gradient [K/cm]	5951	6667	Thermal gradient increases with bead count
Melt Pool Area [mm <sup>2</sup> ]	2.99	1.59	Melt pool area decreases with bead count
$\alpha$ -lath Width [ $\mu$ m]	0.50	0.72	$\alpha$ -lath thickness increases with bead count

Based on Table 3 above,  $\alpha$ -lath thicknesses are generally larger when thermal gradients are lower, and  $\alpha$ -lath thicknesses are also larger for increased melt pool areas. Consideration of the dimensionless thermal gradient and dimensionless cooling rate used by Bontha et al. [12] reveals that the thermal gradient in the horizontal (layer) direction scales with cooling rate. Recent unpublished theoretical work has also shown that the trailing edge thermal gradient at the solidus-liquidus interface occurs strictly in the horizontal (layer) direction at the top surface of the melt pool. Thus, this particular thermal gradient data, which was collected and from a downward-facing thermal imaging camera and computed at the top of the melt pool, can be interpreted in the same way as a cooling rate for trend identification purposes since the velocity of the beam used in this experiment was constant. Therefore,  $\alpha$ -lath thicknesses appear to be larger when cooling rates are lower and smaller when cooling rates are higher, an intuitive result.

In each of the tables above, thermal gradient increases as the melt pool area decreases. Noting Gockel & Beuth showed that lines of constant melt pool area correspond to lines of constant  $\beta$  grain size for wire-feed AM Ti-6Al-4V [1], it appears that larger melt pool areas correspond not only to enlarged  $\beta$  grain sizes but also to thicker  $\alpha$ -laths within those grains. Inspection of Table 4 and Table 5 reveals that  $\alpha$ -lath thicknesses increase with the number of beads used per layer and decrease with pause length. Both an increase in number of beads and a decrease in pause length correspond to an increase in the heat available in the system, providing a mechanism for continued  $\alpha$ -lath growth.

It should be noted, however, that though these trends exist it can also be observed from inspection of the data that neither thermal gradient or melt pool area are sufficient to predict lath thicknesses. For example, the measured thermal gradients from the three-bead leg of the zero second dwell sample increased from region 1 to region 2; a result that is inconsistent with the other three sample legs. Another anomalous comparison can be observed from the three-bead leg of the four second dwell sample, where thermal gradients of 6925 and 6893 K/cm were observed in region 1 and region 2, respectively, while alpha lath widths were computed to be 0.41 and 0.67  $\mu\text{m}$ . This suggests that more work is necessary to properly correlate in situ thermal measurements to  $\alpha$  microstructures in AM processes, perhaps by considering thermal history below the  $\beta$  transus when lath growth is expected to be active.

## 8 Conclusions

This study presents a general framework for quantitative analysis of sub-beta-grain level Widmanstätten  $\alpha$  microstructures in AM Ti-6Al-4V. The methodology includes techniques for analyzing  $\alpha$ -laths of various sizes, as well as an uncertainty quantification tool for comparing inverse linear intercept distributions in various regions of AM components. The quantitative results agree with qualitative visual analysis, and favorably correspond to published theoretical and experimental results. In confirming intuitive trends between thermal gradient, melt pool

size, and solidification microstructure, this work provides a quantitative means for verifying intuition about  $\alpha$ -level structure in AM Ti-6Al-4V. However, although trends were identified, it was also observed that the neither thermal gradient or melt pool size alone is sufficient to predict  $\alpha$ -lath thicknesses, and thus additional research is required to further understand the complex thermal cycles present in AM-fabricated structures.

## 9 Acknowledgements

This material is based in part on research sponsored by Air Force Research Laboratory through America Makes under agreement number FA8650-12-2-7230. The U.S. Government is authorized to reproduce and distribute reprints for Governmental purposes notwithstanding any copyright notation thereon. The views and conclusions contained herein are those of the authors and should not be interpreted as necessarily representing the official policies or endorsements, either expressed or implied, of Air Force Research Laboratory or the U.S. Government.

## 10 References

- 1 Beuth, J., Fox, J., Gockel, J., Montgomery, C., Yang, R., Qiao, H., Soylemez, E., Reeseewatt, P., Anvari, A., Narra, S., and Klingbeil, N., "Process Mapping Across Multiple Direct Metal Additive Manufacturing Processes," in *Solid Freeform Fabrication Proceedings*, Austin, 2013, pp. 655-665.
- 2 Klingbeil, N. W., Zinn, J. W., and Beuth, J. L., "Measurement of residual stresses in parts created by shape deposition manufacturing," in *Solid Freeform Fabrication Proceedings*, Austin, 1997, pp. 125-132.
- 3 Klingbeil, N. W., Beuth, J. L., Chin, R. K., and Amon, C. H., "Measurement and modeling of residual stress-induced warping in direct metal deposition processes," in *Solid Freeform Fabrication Proceedings*, Austin, 1998, pp. 367-374.
- 4 Ong, R., Beuth, J. L., and Weiss, L. E. "Residual stress control issues for thermal deposition of polymers in SFF processes," in *Solid Freeform Fabrication Proceedings*, Austin, 2000, pp. 209-218.
- 5 Klingbeil, N. W., Beuth, J. L., Chin, R. K., and Amon, C. H., "Residual stress-induced warping in direct metal solid freeform fabrication," *International Journal of Mechanical Sciences*, Vol. 44, 2002, pp. 57-77.
- 6 Vasinonta, A., Beuth, J. L., and Griffith, M., "Process maps for predicting residual stress and melt pool size in the laser-based fabrication of thin-walled structures," *Journal of Manufacturing Science and Engineering*, Vol. 129, Issue 1, 2007 pp. 101-109.
- 7 Vasinonta, A., Beuth, J. L., and Ong, R., "Melt pool size control in thin-walled and bulky parts via process maps," in *Solid Freeform Fabrication Proceedings*, Austin, 2001, pp. 432-440.

- 8 Vasinonta, A., Beuth, J. L., and Griffith, M., "A Process Map for Consistent Build Conditions in the Solid Freeform Fabrication of Thin-Walled Structures," *ASME Journal of Manufacturing Science and Engineering*, Vol. 123, pp. 615-622, 2001.
- 9 Vasinonta, A., Beuth, J. L., and Griffith, M., "Process Maps for Laser Deposition of Thin-Walled Structures," in *Solid Freeform Fabrication Proceedings*, Austin, 1999, pp. 383-391.
- 10 Klingbeil, N. W., Brown, C., Bontha, S., Kobryn, P., and Fraser, H., "Prediction of Microstructure in Laser Deposition of Titanium Alloys," in *Solid Freeform Fabrication Proceedings*, Austin, 2002, pp. 142-149.
- 11 Klingbeil, N. W., Bontha, S., Brown, C. J., Gaddam, D. R., Kobryn, P. A., Fraser, H. L., Sears, J. W., "Effects of Process Variables and Size Scale on Solidification Microstructure in Laser-Based Solid Freeform Fabrication of Ti-6Al-4V," in *Solid Freeform Fabrication Proceedings*, Austin, 2004, pp. 92-103.
- 12 Bontha, S. and Klingbeil, N.W., "Thermal Process Maps for Controlling Microstructure in Laser-Based Solid Freeform Fabrication," *Solid Freeform Fabrication Proceedings*, pp. 219-226, 2003.
- 13 Bontha, S., Klingbeil, N.W, Kobryn, P., and Fraser, H.L., "Effects of Process Variables and Size Scale on Solidification Microstructure in Beam-Based Fabrication of Bulky 3D Structures," *Materials Science and Engineering A*, vol. 513-514, 2009, pp. 311-318.
- 14 Bontha, S., Klingbeil, N.W, Kobryn, P., and Fraser, H.L., "Thermal Process Maps for Predicting Solidification Microstructure in Laser Fabrication of Thin Wall Structures," *Journal of Materials Processing Technology*, vol. 178, 2006, pp. 135-142.
- 15 Davis, J., Klingbeil, N., and Bontha, S., "Effect of Free-Edges on Melt Pool Geometry and Solidification Microstructure in Beam-Based Fabrication of Bulky 3-D Structures," in *Solid Freeform Fabrication Proceedings*, Austin, 2010, pp. 230-241.
- 16 Davis, J., Klingbeil, N., and Bontha, S., "Effect of Free-Edges on Melt Pool Geometry and Solidification in Beam-Based Fabrication of Thin-Wall Structures," in *Solid Freeform Fabrication Proceedings*, Austin, 2009, pp. 320-331.
- 17 Beuth, J. L., "Methods for Determining Process Variable Combinations Yielding Constant Melt Pool Geometry for Single Bead Deposits in Direct Digital Manufacturing," *Materials Science and Technology*, Vol. 31, Issue 8, June 2015, pp. 912-916.
- 18 Gockel, J., and Beuth, J., "Understanding Ti-6Al-4V Microstructure Control in Additive Manufacturing via Process Maps," in *Solid Freeform Fabrication Proceedings*, Austin, 2013, pp. 666-674.
- 19 Purtonen, T., Kalliosaari, A., Salminen, A., "Monitoring and adaptive control of laser processes," *Physics Procedia*, Volume 56, 2014, pp. 1218-1231.
- 20 Reutzel, Edward W., Nassar, Abdalla R., "A survey of sensing and control systems for machine and process monitoring of directed-energy, metal-based additive manufacturing," *Rapid Prototyping Journal*, Vol. 21, Issue 2, 2015, pp.159-167.
- 21 Griffith, M. L., Schlienger, M. E., Harwell, L. D., Oliver, M. S., Baldwin, M. D., Ensz, M. T., Essien, M., Brooks, J., Robino, C. V., Smugeresky, J., Hofmeister, W. H., Wert, M. J.,

- Nelson, D. V., "Understanding thermal behavior in the LENS process," *Materials & Design*, Vol. 20, Issue 2, June 1999, pp. 107–113.
- 22 Hofmeister, W., Knorovsky, G.A., MacCallum, D.O., "Video monitoring and control of the LENS process," *AWS 9<sup>th</sup> International Conference on Computer Technology in Welding Proceedings*, 1999, pp. 417-424.
  - 23 Hofmeister, W., Griffith, M., Ensz, M., Smugeresky, J., "Solidification in direct metal deposition by LENS processing," *Journal of Materials*, Vol. 53, Issue 9, 2001, pp. 30–34.
  - 24 Wu, X., Liang, J., Mei, J., Mitchell, C., Goodwin, P., Voice, W., "Microstructures of laser-deposited Ti–6Al–4V," *Materials & Design*, Vol. 25, Issue 2, 2004, pp. 137–144.
  - 25 Brandl, E., Leyens, C., Palm, F., "Mechanical properties of additive manufactured Ti–6Al–4V using wire and powder based processes," *Materials Science and Engineering*, Vol. 26, 2011.
  - 26 Brandl, E., Michailov, V., Viehweger, B., Leyens, C., "Deposition of Ti–6Al–4V using laser and wire, part I: Microstructural properties of single beads," *Surface and Coatings Technology*, Vol. 206, Issue 6, December 2011, pp. 1120–1129.
  - 27 Kelly, S. M., Kampe, S. L., "Microstructural evolution in laser-deposited multilayer Ti-6Al-4V builds: Part I. Microstructural characterization," *Metallurgical and Materials Transactions A*, Vol. 35, Issue 6, June 2004, pp. 1861-1867.
  - 28 Kelly, S. M., Kampe, S. L., "Microstructural evolution in laser-deposited multilayer Ti-6Al-4V builds: Part II. Thermal Modeling," *Metallurgical and Materials Transactions A*, Vol. 35, Issue 6, June 2004, pp. 1869-1879.
  - 29 Collins, P. C., Welk, B., Searles, T., Tiley, J., Russ, J. C., Fraser, H. L., "Development of methods for the quantification of microstructural features in  $\alpha+\beta$ -processed  $\alpha/\beta$  titanium alloys," *Materials Science and Engineering A*, Issue 508, 2009, pp. 174-182.
  - 30 Sosa, J. M., Huber, D. E., Welk, B., and Fraser, H. L., "Development and application of MIPAR: a novel software package for two- and three-dimensional microstructural characterization," *Integrating Materials and Manufacturing Innovation*, Vol. 3, Issue 10, April 2014.
  - 31 Gundersen, H. J. G., Jensen, T.B., and Osterby, R., "Distribution of membrane thickness determined by lineal analysis," *Journal of Microscopy*, Vol. 113, May 1978, pp. 27-43.
  - 32 Cha, S., "Comprehensive Survey on Distance/Similarity Measures between Probability Density Function," *International Journal of Mathematical Models and Methods in Applied Sciences*, Vol. 1 Issue 4, 2007, pp. 300-307.
  - 33 Kriczky, D. A., Irwin, J., Reutzel, E. D., Michaleris, P., Nassar, A. B., Craig, J., "3D spatial resolution of thermal characteristics in directed energy deposition through optical thermal imaging," *Journal of Materials Processing Technology*, Vol. 221, July 2015, pp. 172-186.
  - 34 Loughnane, G., Groeber, M., Uchic, M., Shah, M., Srinivasan, R., Grandhi, R., "Modeling the effect of voxel resolution on the accuracy of phantom grain ensemble statistics," *Materials Characterization*, Vol. 90, April 2014, pp. 136-150.
  - 35 Donachie, M. J., *Titanium: A Technical Guide*. ASM International, 2000.